

Supporting Information:

Dissecting the nature and dynamics of electronic excitations in a solid-state aggregate of a representative non-fullerene acceptor

Samuele Giannini,^{*a} Jesús Cerdá,^b Giacomo Prampolini,^a Fabrizio Santoro^a, David Beljonne^b

a) Institute of Chemistry of OrganoMetallic Compounds, National Research Council (ICCOM-CNR), I-56124 Pisa, Italy

b) Laboratory for Chemistry of Novel Materials, University of Mons, Mons 7000, Belgium

Email : samuele.giannini@cnr.it

Section S1: Excitation energies

Table S1: Excitation energy (eV) and oscillator strength (f) for the lowest-energy (singlet) states (S1 and S2). Basis set fixed at 6-31G(d,p) level.

	S1 vert	f	S1 adiab	S2 ver	f	S1 exp
CAM-B3LYP	2.26	2.692	2.10	2.86	0.000	
wB97XD	2.35	2.717	2.17	2.92	0.000	
LC- ω hPBE ^a	1.99	2.618	1.90	2.56	0.000	
CAM-B3LYP (CHCl ₃) ^b	2.08	3.128	1.86	2.63	0.000	1.66
LC- ω hPBE (CHCl ₃) ^c	1.85	2.474	1.79	2.27	0.00	

^aLC- ω hPBE indicates an optimally-tuned range-separated hybrid (RSH) functional.¹ The non-empirical tuning procedure adopted in this work is described elsewhere²⁻⁴ and the OT ω value was found at 0.0850 Bohr⁻¹ for the m-4TICO molecule by using the LC- ω hPBE functional and the 6-31G(d,p) basis set.³ ^bA solvent screening has been added using a Polarizable Continuum Model with constants characteristic of Chloroform. ^cThe optimally tuned LC- ω hPBE has been screened with a by changing the screening part of the functional according to the macroscopic dielectric constant of the solvent, without altering the OT ω value (tuned in gas-phase).²

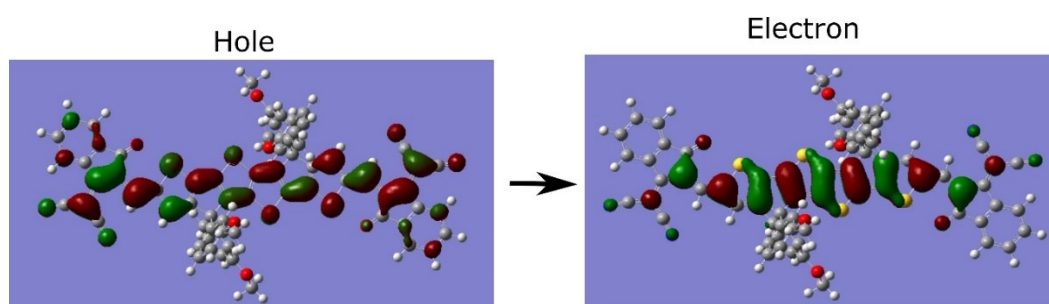


Figure S1: Natural transition orbitals (NTOs) for the first singlet excited state at CAM-B3LYP/6-31G(d,p) level of theory. Alkyl-side chains are removed.

Section S2: Relaxation energies and Huang-Rhys factors

The internal relaxation energies associated with the excitation of m-4TICO was evaluated using energy differences at different points on the Potential Energy Surfaces (PES) of ground and the excited S1 state, (see for example in Ref.⁵):

$$\lambda_{EX}^{\text{rel}} = E_{EX}(\mathbf{R}_N) - E_{EX}(\mathbf{R}_{EX}) \quad (\text{S1})$$

$$\lambda_N^{\text{rel}} = E_N(\mathbf{R}_{EX}) - E_N(\mathbf{R}_N) \quad (\text{S2})$$

$\lambda_{EX}^{\text{rel}}$ and λ_N^{rel} are the relaxation energies of the excited and ground (neutral) states, respectively. $E_{EX(N)}(\mathbf{R}_{N(EX)})$ is the energy of the excited (neutral) molecule in the optimized neutral (excited) state and $E_{EX(N)}(\mathbf{R}_{EX(N)})$ is the energy of excited (neutral) molecule in the optimized excited (neutral) minimum. We note in passing that the total reorganization energy commonly used in Marcus theory⁶, λ , is the sum of both relaxation energies in Eqs S1 and S2, namely $\lambda = \lambda_{EX}^{\text{rel}} + \lambda_N^{\text{rel}}$. These values were computed using the levels of theory reported in Table S2. Exciton relaxation energies are quite robust with choice of the DFT functional and change very little depending on the approximation of the excited state potential energy surface, as we describe below.

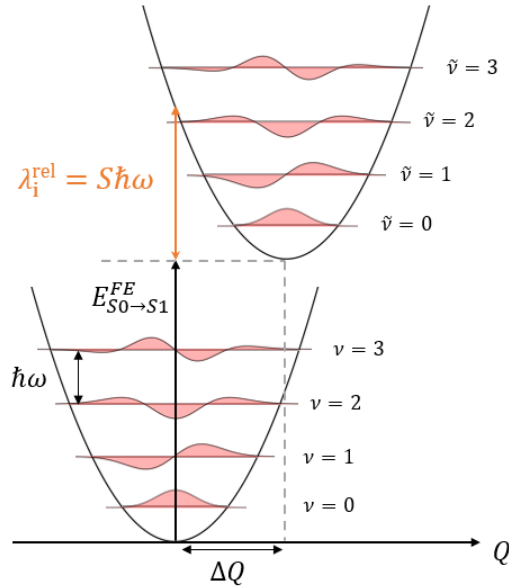


Figure S2: Harmonic nuclear potential wells for ground and excited states. The excited state potential is shifted relative to the ground state potential by ΔQ .

A complementary useful approach to calculate the relaxation energies of excited and ground states and to determine the parameters required to construct the Frenkel Hamiltonian in Eq. 1 of the main text (namely, the Huang-Rhys factor and effective frequency) involves their decomposition into contributions relative to each normal mode (schematized in Fig. S2 for two harmonic potential and a single mode). This method is herein referred to as normal mode analysis (NMA). The total relaxation energy of the excited and neutral state can be written as a sum of the individual contributions (see Fig. S3):

$$\lambda_{N(EX)}^{\text{rel}} \cong \sum_i \hbar\omega_i S_i \quad (\text{S3})$$

where S_i denotes the Huang-Rhys factor of a specific mode of frequency $\hbar\omega_i$ of the normal modes of the ground or excited state, respectively.

To calculate Eq. S3, we employ harmonic potential energy surfaces adopting FCclasses3.0.⁷ Specifically, we tested different ways of approximating the excited state potential energy surface (PES), namely the Vertical Hessian (VH), Adiabatic Hessian (AH) approaches and Adiabatic Shift (AS) approaches. We note that, to correctly approximating the low frequency torsional modes, internal curvilinear coordinates are used. In VH approach a quadratic model of the final state PES is built starting from geometry, energy, gradient and Hessian of the excited state at the Franck-Condon point. Instead in AH, the final PES is expanded around its own equilibrium structure found after excited state optimization. This allows us to calculate gradient and Hessian matrix at the minimum of the excited state potential and reconstruct the excited state PES by taking into account Duschinsky's normal mode transformation.⁸ AS is a further approximate but yet useful model built by assuming that the final and initial state PES share the same Hessian (i.e. the same normal modes and frequencies) and their minima are simply displaced (Fig. S3). In Table S2, we note that for our system, AS, AH and VH approaches provide similar results, and they also agree with the relaxation energy calculated with Eq. S1 and S2. This suggests that the PES are well represented in the harmonic approximation.

Table S2: Excitation relaxation energies (eV) from Eq. S1 and S2 and normal mode analysis (NMA)

	CAM-B3LYP		wB97X-D	
	λ_N^{rel}	$\lambda_{EX}^{\text{rel}}$	λ_N^{rel}	$\lambda_{EX}^{\text{rel}}$
2-POINTS	0.163	0.165	0.180	0.178
NMA (VH)	0.169	0.166	0.188	0.180
NMA(AH)	0.167	0.165	0.184	0.179
NMA (AS)	0.167	0.167	0.184	0.184

According to the NMA the vector of the displacement between the neutral and excited state is projected onto the normal modes of the molecule. This allows us to partition the relaxation energies into mode contributions as represented in Fig. S4. And to calculate the Huang-Rhys factor of each mode.

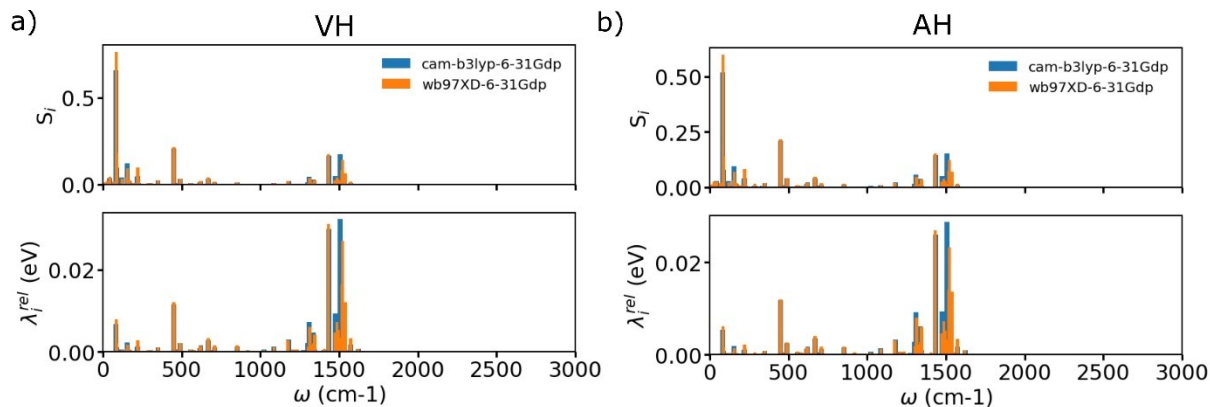


Figure S3: Huang-Rhys factors (top panels) and relaxation energies (bottom panels) when going from the ground to the excited state geometry in the Vertical Hessian (VH) approach in **a)** and Adiabatic Hessian approach in **b)**.

In Fig. S3, we show that the relaxation energies associated with the excitation involve vibrational frequencies that are essentially located above 1300 cm⁻¹. Thus, as done by others,⁹ we assumed that part of the total relaxation energy associated to the formation of an excited state is carried out by a single high-frequency mode with an effective frequency $\hbar\omega_{\text{eff}}$. This quantity was evaluated for each excitation by weighting the frequencies of each mode across the spectrum above 1300 cm⁻¹ in Fig. S3 by the corresponding Huang-Rhys factor S_i , namely $\hbar\omega_{\text{eff}} = \sum_i \hbar\omega_i S_i / \sum_i S_i$. The effective Huang-Rhys factor associated to the high-frequency relaxation energy ($\lambda_{\text{hf}}^{\text{rel}}$) becomes $S_{\text{eff}} = \lambda_{\text{hf}}^{\text{rel}} / \hbar\omega_{\text{eff}}$. A summary of the parameters used to build the Hamiltonian in Eq. 1 for solid-state aggregates is reported in Table S3. The rest of the relaxation energy associated with low-frequency modes ($\lambda_{\text{lf}}^{\text{rel}}$) was assumed to be classical and,

thus, to contribute to the homogeneous broadening of the spectrum ($\sigma^{\text{hom.}} = \sqrt{2K_B T \lambda_{\text{lf}}^{\text{rel}}} = 51$ meV). The quality of the effective Huang-Rhys factor obtained from this procedure is checked against the experimental measurement of the spectrum (see Fig. 2 in the main text). This is possible since experimentally the Huang-Rhys factor is related to the ratio between the intensity of the first vibronic band and the Franck-Condon (FC) transition by $S_{\text{exp}} = \frac{I_{1-0}^{\text{vib}}}{I_{0-0}^{\text{vib}}}$.¹⁰ The experimental value $S_{\text{exp}} = 0.62$ obtained for the optical absorption spectrum in Chloroform solution agrees well with our computed estimate. Moreover, our results are also consistent with what previously found in Ref.¹¹ for other NFA molecules.

Table S3: Relaxation energies (in eV) and Frenkel Exciton parameters at CAM-B3LYP/6-31G(d,p) level of theory.

λ^{rel}	0.167
$\lambda_{\text{hf}}^{\text{rel}}$	0.116
$\lambda_{\text{lf}}^{\text{rel}}$	0.051
$\hbar\omega_{\text{eff}}$	0.180
S_{eff}	0.646
$\sqrt{S_{\text{eff}}}$	0.804

Section S3: Crystal Structure

The crystal structure of m-4TICO used in this work was taken from Ref.¹² The unit cell contains one molecules ($Z = 1$) in the cell and lattice parameters are reported in Table S4.

Table S4: Unit cell parameters (Å) and cell vectors (degrees).

CCDC code	a	b	c	α	β	γ
VUBJIO	8.6526	16.4878	18.0435	114.697	103.822	90.89

The unit cell was replicated to build supercells of different sizes to study optical and transport properties. Different cell sizes have been considered to check for convergence of optical and transport properties.

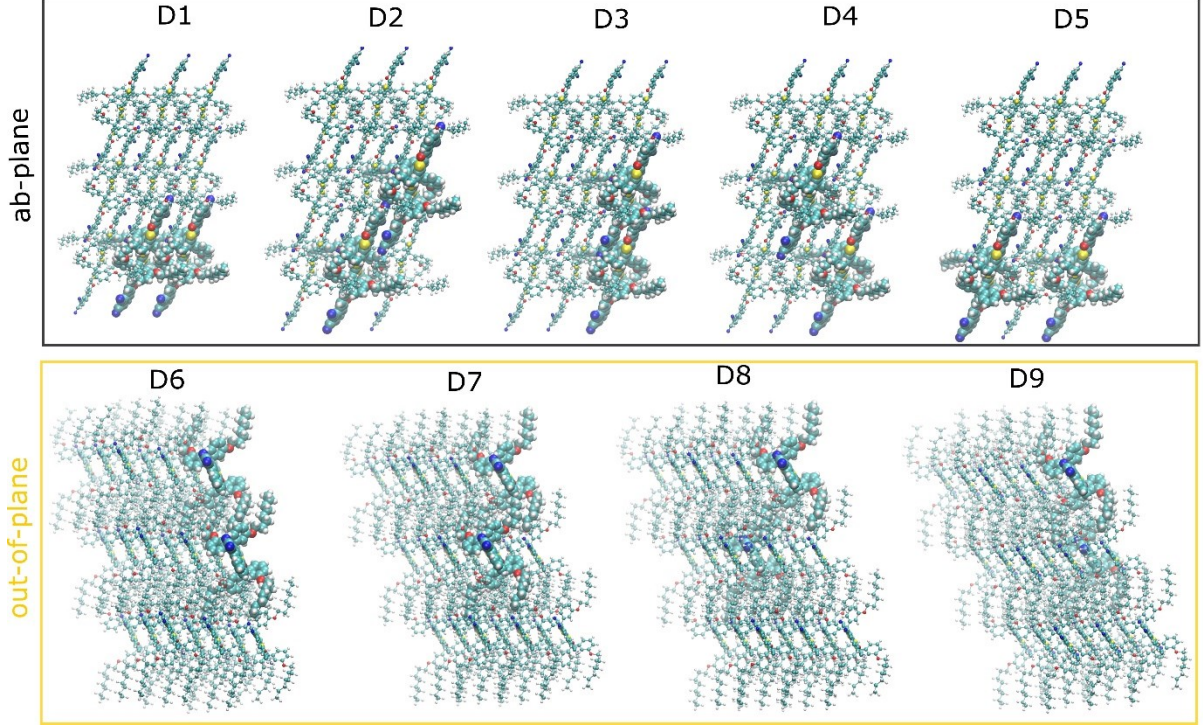


Figure S4: m-4TICO unique dimers with COM distance within 20 Å extracted from a 3x3x3 supercell. Dimers are classified as within the *a-b* plane and out-of-plane interactions.

Section S4: Absorption and Emission spectrum

The normalized absorption spectrum is calculated by using^{10,13}:

$$A(\omega) = \frac{1}{N} \sum_j \omega_j |\langle \Psi^{(g)} | \hat{\mu} | \Psi^{(j)} \rangle|^2 W(\omega - \omega_j) \quad (\text{S4})$$

where $\hat{\mu}$ is the transition dipole moment operator between the ground state wavefunction $\Psi^{(g)}$ and a given eigenstate $\Psi^{(j)}$ of the system, W is a line broadening function which in this work is taken to be a Gaussian function with a standard deviation σ , and ω_j is the excitation energy of each j state. The line intensity is the oscillator strength calculated as the product of the square of the transition dipole moment and the transition energy (ω_j). For the aggregate, the dipole moment operator acting on the excitonic wavefunction gives an excitonic dipole (Eq. S7).

The emission spectrum is calculated analogously by using^{10,13}:

$$S(\omega) = \sum_j \frac{e^{-(\omega_j - \omega_{j=0})/k_B T}}{\sum_j e^{-(\omega_j - \omega_{j=0})/k_B T}} \sum_{v_i=0,1,2} (\omega_j - v_i \omega_{\text{eff}})^3 I_{\square}^{v_i} W(\omega - \omega_j + v_i \omega_{\text{eff}}) \quad (\text{S5})$$

where the first sum runs over the adiabatic excited states (j) of the system that are Boltzmann averaged to consider the temperature effect in emission (which otherwise would take place only from the lowest energy excited state). The emission terminates on the ground electronic state creating a vibronic progression with peak frequencies at $\omega_j + \nu_i \omega_{\text{eff}}$ (where ν_i is the number of total vibrational quanta). $I_{\text{vib}}^{\nu_i}$ represents the intensity of the peaks whose explicit mathematical expressions are given in Ref.¹³.

The previous Eqs S4 and S5 have been used to obtain the optical spectra shown in the main text for both single molecule and solid-state aggregate by considering a single effective mode coupled to the excitation of each site. To check that this is indeed a meaningful approximation, we calculated the single molecule spectrum considering all normal modes of the molecule introduced as displaced harmonic oscillators. The Franck-Condon factor were calculated using the implementation in FCclasses3.0.⁷ As represented in Fig. S5, the 0-1 vibronic shoulder is indeed due to essentially two high-frequency vinyl stretching modes with very similar frequency (see Fig. S5a,b). Lower frequency torsional modes, for instance the mode 26 in Fig. S5, is responsible for the broadening of the first 0-0 band. We conclude that considering only a single effective mode per molecular site in this system provides a useful approximation.^{10,14}

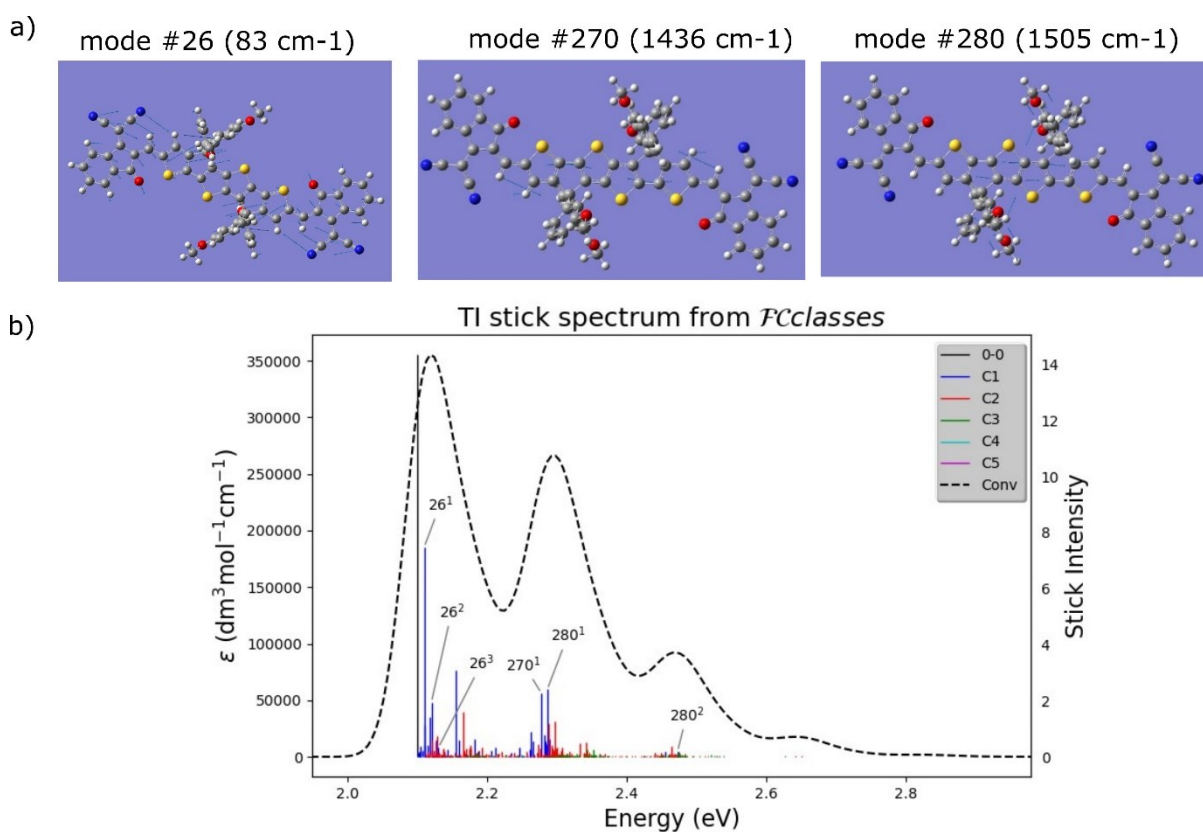


Figure S5: **a)** Representation of the normal modes more strongly coupled to the excitation S0-S1. **b)** Vibronic spectrum of m-4TICO constructed considering all the molecular normal modes (and using the Time Independent approach as described in Ref.⁷). The excitation classes⁷ are represented with different colours.

Section S5: Frenkel Exciton basis set

Spano et al. previously introduced a multiparticle basis set that effectively describes excitonic eigenstates of a system across weak to intermediate exciton coupling regimes.^{10,13} In this context, "particle" refers to a chromophore that supports either a combined electronic and vibrational excitation, or solely a vibrational excitation. In our analysis, we focus on excitations involving a single molecule promoted to an electronically excited state.

Accurate calculations are obtainable by making the one (1p) or two-particle (2p) approximation in which the basis set in which the Hamiltonian in Eq. 1 of the main text is truncated. The truncation consists in considering only one electronic excitation with its own vibrations (1p) or two-particle states with one state electronically and vibrationally excited states and the other with vibrational excitation taking place in the ground state of another molecule. The 1p wavefunction is given in Eq. 7 of the main text, while the 2p wavefunction of an eigenstate of the 2p Hamiltonian is given here as:

$$|\Psi^{(j)}\rangle = |\Psi_{1p}^{(j)}\rangle + |\Psi_{2p}^{(j)}\rangle = \sum_k \sum_{\tilde{\nu}=0}^{\nu_{\max}} c_{k,\tilde{\nu}}^{(j)} |e_k, \tilde{\nu}_k\rangle + \sum_k \sum_{l \neq k} \sum_{\tilde{\nu}=0}^{\nu_{\max}-1} \sum_{\nu=1}^{\nu_{\max}-\tilde{\nu}} c_{k,\tilde{\nu},l,\nu}^{(j)} |e_k, \tilde{\nu}_k; g_l, \nu_l\rangle \quad (\text{S6})$$

where the first two terms correspond to one- and two-particle FE excitations, respectively, with $\tilde{\nu}$ and ν representing the vibrational energy levels in the shifted excited state potential and ground state potential respectively, ν_{\max} is the maximum number of vibrational levels considered for the effective mode coupled to the singlet excitations on the different molecules. Once defined in each basis set, the wavefunction can be normalized.

According to the Franck-Condon principle, the transition dipole moment contains vibrational overlap factors between the ground state $|\Psi^{(g)}\rangle$ and the excited state $|\Psi^{(j)}\rangle$. Since two-particle states include a vibrational excitation in the electronic ground state, these give rise to a factor of zero, thus we have:

$$\langle \Psi^{(g)} | \hat{\mu} | \Psi^{(j)} \rangle = \sum_k \sum_{\tilde{\nu}=0}^{\nu_{\max}} \boldsymbol{\mu}_k c_{k,\tilde{\nu}}^{(j)} \langle \Psi^{(g)} | e_k, \tilde{\nu}_k \rangle = \sum_k \sum_{\tilde{\nu}=0}^{\nu_{\max}} \boldsymbol{\mu}_k c_{k,\tilde{\nu}}^{(j)} f_{0,\tilde{\nu}} \quad (\text{S7})$$

Where, $f_{0,\tilde{\nu}}$ is the Franck-Condon factor between the ground and excited vibrational state.

Section S6: Calculation of Excitonic couplings

We tested various methods of computing excitonic couplings as outlined in the main text to find a balance between accuracy and feasibility for a large number of snapshots and molecular pairs. The electronic coupling plays a critical role in the Frenkel exciton Hamiltonian in Eq. 2. We have computed excitonic couplings by employing the full Coulomb integral ($V_{kl}^{\text{Coul.}}$) as presented in Eq. 3 of the main text, the transition electric field (TrESP) method (V_{kl}^{TrESP}) in Eq. 4, and the point-dipole approximation (PDA, V_{kl}^{PDA}) in Eq. S8 for the systems under consideration. These results were compared to the overall excitonic coupling value (V_{kl}^{Tot}), derived using the multi-state fragment excitation difference fragment charge difference approach (MS-FED-FCD) described subsequently.

MS-FED-FCD methodology

The MS-FED-FCD extends the capabilities of the previously developed diabaticization schemes such as the 2-state fragment excitation difference (FED)¹⁵ and fragment charge difference (FCD)^{16,17} approaches. All these methods, which have been described in detail elsewhere¹⁸⁻²¹, involved the partition of a given donor acceptor pair into two fragments and by using appropriate additional operators, the adiabatic Hamiltonian of the dimer (formed by two or more adiabatic states of the system) is transformed into a diabatic basis, which allows a direct evaluation of the couplings between FE states or charge transfer (CT) states from the diabatic Hamiltonian matrix. When dealing with closely packed molecules, the adiabatic states of the interacting pair might be partially mixed with several states of different characters (*e.g.*, FE and CT excitons). This is where the MS-FED-FCD is particularly useful and goes beyond standard FED and FCD algorithms, which only allow to diabaticize two states at a time (*i.e.*, two FEs or two CTs respectively). Specifically, MS-FED-FCD allows us to include several adiabatic excited states of the donor-acceptor system in the diabaticization procedure to ensure a complete de-mixing between excitations of different nature and an optimal reconstruction of the localized FE and CT states, even in cases where a given adiabatic state is the combination of many diabatic states of both donor and acceptor.

In Table S5, we demonstrate that in m-4TICO the energy of the CT states is much higher than the energy of the FE states even for the closest pairs. In addition, the coupling between the FE and CT states is significantly smaller than the couplings between FE states. Overall, this means that in this system CT excitations are unlikely to play a significant role on the optical and dynamical properties of this system (conversely to what happens in other NFAs like Y6²²). This is in line with what has been recently found for the analogue ITIC system.²³

Table S5: Computed diabatic energies of FE and CT states and related (absolute value) excitonic couplings of the nearest neighbour pairs of m-4TICO molecules. Energies are in eV, couplings in meV and distances in Å.

Dimer	Distance	CT energy	FE energy	$ V_{kl}^{\text{FE-CT}} $	$ V_{kl}^{\text{FE-FE}} $
D1	8.65	3.12	2.22	1.0	59.9
D2	18.74	2.89	2.17	13.7	49.8
D3	16.49	2.96	2.19	23.7	29.6
D4	18.50	3.41	2.20	0.0	5.4
D5	17.31	3.46	2.21	0.0	17.7
D6	18.04	3.48	2.21	0.0	16.3
D7	18.05	3.46	2.20	0.0	15.0
D8	18.56	3.47	2.20	0.0	13.6
D9	18.68	3.44	2.20	0.0	12.2

Transition ESP charges

Despite the usefulness of the MS-FED-FCD, its relatively high computational cost makes it impractical to compute long-range excitonic interactions between all pairs in a super cell of a large molecular aggregate (as the ones considered in this work). An alternative, approximate approach that has proven valuable to calculate Coulombic interactions in very good agreement with MS-FED-FCD in a number of organic crystals²¹ relies on the interaction between

transition charges obtained from the fitting of the electrostatic potential (TrESP) in Eq. 4 in the main text.

We verified the accuracy of the TrESP charges obtained via the electrostatic potential (ESP) fitting method (detailed in the main text) by ensuring that the total of the TrESP charges equals zero (mimicking the integration of the full transition density over all space) and that the dipole moments calculated from the charge densities match those derived from the atomic TrESP charges. V_{kl}^{TrESP} obtained by using the ESP fitting procedure described in the Method section is in very good agreement with $V_{kl}^{\text{Coul.}}$ for all crystal pairs investigated (see Table S6 and 1 in the main text).

In Table S6, we report the comparison of the excitonic couplings evaluated with two different level of theory (i.e. wB97X-D and CAM-B3LYP) and related TrESP couplings. Both levels of theory give comparable couplings, underscoring the fact that these excitonic interactions are primarily influenced by the shape of the interacting transition densities, but not as much by the energetics of the interacting states. Note that the sign in Table S6 is consistently given for all the interactions and among different pairs with H-like interaction being positive and J-like interaction negative. The excitonic dipoles of the molecules in m-4TICO crystal are oriented all in the same direction by construction since m-4TICO has only one molecule per unit cell that is being periodically replicated.

Table S6: Computed excitonic couplings of the nearest neighbour pairs of m-4TICO molecules. All couplings in meV and distances in Å.

Dimer	Distance	CAM-B3LYP		wB97XD	
		$V_{kl}^{\text{Coul.}}$	V_{kl}^{TrESP}	$V_{kl}^{\text{Coul.}}$	V_{kl}^{TrESP}
D1	8.65	59.70	59.64	58.24	58.18
D2	18.74	-47.27	-47.16	-45.05	-44.93
D3	16.49	-26.83	-26.80	-25.15	-25.11
D4	18.50	4.98	4.98	4.81	4.81
D5	17.31	17.65	17.64	17.28	17.27
D6	18.04	16.39	16.39	15.83	15.83
D7	18.05	13.95	13.96	13.40	13.40
D8	18.56	13.52	13.53	13.35	13.37
D9	18.68	12.40	12.40	12.42	12.43

Because the TrESP charges are calculated only once at a reference geometry a possible downside of this approach is that although the structural fluctuations modify the TrESP coupling in Eq. 4 via the inverse distance dependence, the TrESP charges themselves do not change in time. For highly flexible molecules this is potentially a problem as the actual fluctuations of the excitonic couplings could be underestimated in the TrESP procedure. This is only a minor issue with m-4TICO where the “reference” coupling fluctuations given by the $V_{kl}^{\text{Coul.}}$ are already small compared to their mean value because the electronic and transport properties will not be strongly affected. We show this in Table S7, by computing mean value and standard deviation of the coupling fluctuations on 100 snapshots extracted from molecular dynamics with TrESP and the full transition density approaches. Note how the fluctuations or the excitonic couplings are much smaller than the mean values (see Fig. S6). This is very

different compared to the fluctuations of the electronic or hole transfer couplings (see main text for a discussion).^{24,25}

Table S7: Computed excitonic couplings of the three largest nearest neighbour pairs of m-4TICO molecules. All couplings in meV.

	D3		D2		D1	
	V_{kl}^{TrESP}	$V_{kl}^{\text{Coul.}}$	V_{kl}^{TrESP}	$V_{kl}^{\text{Coul.}}$	V_{kl}^{TrESP}	$V_{kl}^{\text{Coul.}}$
$\langle V_{kl}^{\square} \rangle$	-29.78	-21.87	-49.30	-41.42	61.58	52.81
$\sigma_V^{\square a}$	3.93	7.74	2.52	4.23	2.24	4.25

^aDefined as: $\sigma_V^{\square} = \sqrt{\langle (V_{kl}^{\square} - \langle V_{kl}^{\square} \rangle)^2 \rangle}$

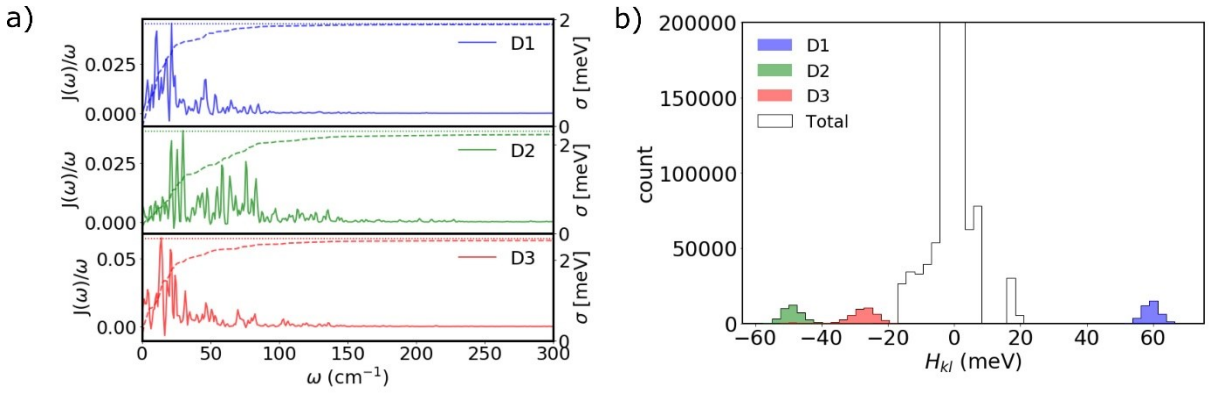


Figure S6: **a)** Spectral density of the largest nearest-neighbour excitonic coupling pairs sampled along a MD dynamic performed on as described in the main text. The equations used are Eq. S9-S11. **b)** Excitonic coupling distributions for all excitonic couplings of a 20x20x1 m-4TICO supercell. The black line indicates the total coupling distribution including long-range couplings, while D1, D2, D3 coupling distributions are coloured.

Point dipole approximation

It is customary in (dipole-based) Förster theory, at sufficiently large distances between sites (i.e. distance larger than the dimension of the interacting molecules), to approximate the transition densities of donor and acceptor the first non-zero term in a multipole expansion, i.e. the transition dipole moment. This approximation is referred to as point dipole approximation (PDA) and the related excitonic coupling, V_{kl}^{PDA} , can be written as:

$$V_{kl}^{\text{PDA}} = \frac{\boldsymbol{\mu}_k \cdot \boldsymbol{\mu}_l}{r_{kl}^3} - \frac{3(\boldsymbol{\mu}_k \cdot \mathbf{r}_{kl})(\boldsymbol{\mu}_l \cdot \mathbf{r}_{kl})}{r_{kl}^5} \quad (\text{S8})$$

where \mathbf{r}_{kl} is the vector distance between k and l molecules and $\boldsymbol{\mu}_k$ and $\boldsymbol{\mu}_l$ their respective transition dipole moments. We found that the PDA approximation breaks down for all pairs of molecules and should not be used (see Table 1 in the main text).

Section S7: Convergence of m-4TICO solid-state spectrum

In Fig. S7, we assess the convergence of the optical spectrum in terms of system size, dielectric screening constant applied to the excitonic interactions and particle basis set truncation.

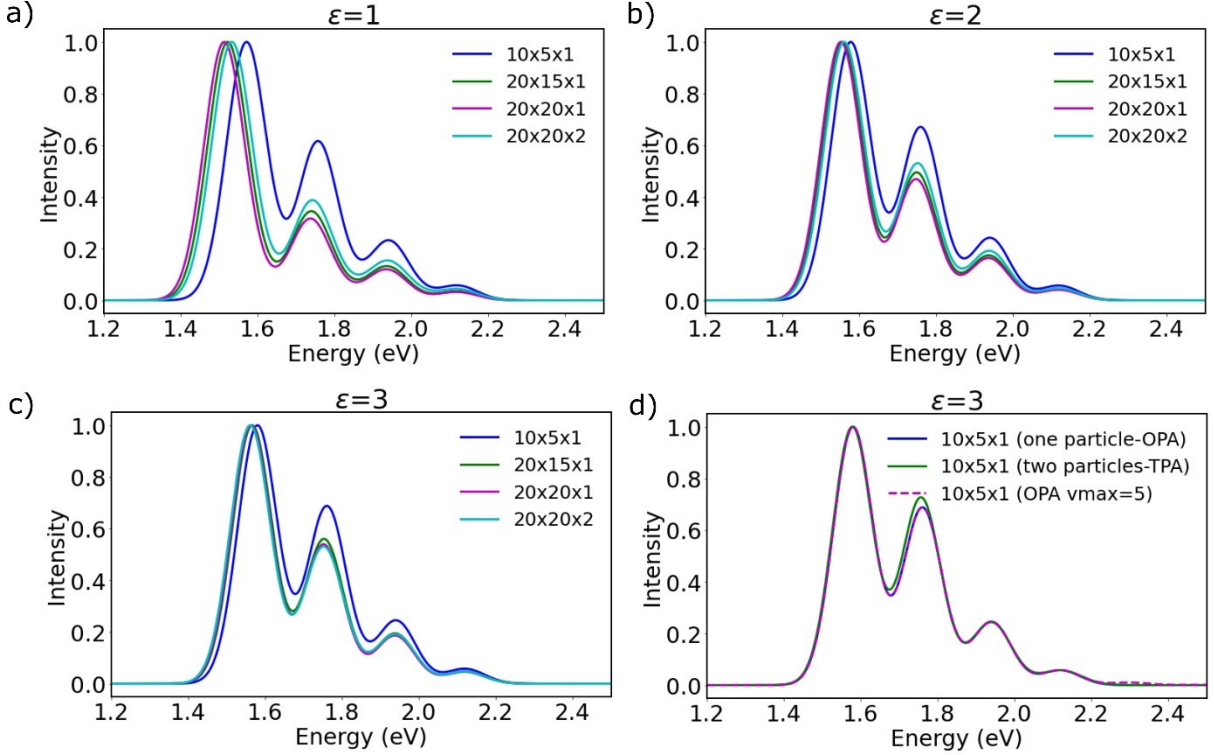


Figure S7: Convergence of the m-4TICO solid-state aggregate spectrum with respect to supercell size with respect to dielectric constant **a)** $\epsilon=1.0$, **b)** $\epsilon=2.0$, **c)** $\epsilon=3.0$. Panel **d)** convergence with respect to one or two particle basis set and number of vibrational energy levels.

Section S8: Spectral density and impact of disorder on m-4TICO solid-state spectrum

The fluctuations associated with a time signal can be analysed using the spectral density approach. Denoting the autocorrelation function of a given time series $J(t)$ as $C_a(t)$, we have:

$$C_a(t) = \langle \delta J(0) \delta J(t) \rangle \quad (\text{S9})$$

where $\delta J(t) = J(t) - \langle J \rangle$. The spectral density function, $S_a(\omega)$, is obtained from the cosine transform of $C_a(t)$ as:

$$\frac{S_a(\omega)}{\omega} = \frac{\beta}{2} \int_0^{+\infty} dt \cos(\omega t) C_a(t) \quad (\text{S10})$$

where $\beta = 1/K_B T$, allowing $C_a(t)$ to be expressed in terms of the inverse transform as:

$$C_a(t) = \frac{4}{\beta\pi} \int_0^{+\infty} d\omega \cos(\omega t) \frac{S_a(\omega)}{\omega} \quad (\text{S11})$$

The autocorrelation function at $t = 0$ is equivalent to the variance of $J(t)$, $C_a(0) = \langle \delta J^2 \rangle = \sigma^2$. So, we can calculate the running integral of Eq. S12 with $t = 0$ up to a frequency ω , which corresponds to the variance of the time series including all frequency contributions up to ω . Working in terms of the root-mean-square fluctuation $\sigma(\omega) = \sqrt{C_a(0)}$, we have:

$$\sigma(\omega) = \left[\frac{4}{\beta\pi} \int_0^{+\omega} d\omega' \frac{S_a(\omega')}{\omega'} \right]^{1/2} \quad (\text{S12})$$

If the signal is related to the excitation energy gap and $J(t) = \Delta E(t)$, one can link the spectral density obtained from an MD at finite temperature to the relaxation energy calculated with Eq. S3. In linear response, one can prove that:

$$\lambda_{\text{rel}}^{\text{rel}} = \frac{\beta}{2} \langle \delta \Delta E^2 \rangle = \frac{2}{\pi} \int_0^{+\omega} d\omega' \frac{S_a(\omega')}{\omega'} \quad (\text{S13})$$

To compare with the NMA at 0K, for each frequency ω (in an infinitesimal interval) the relaxation energy becomes:

$$\lambda_{\text{rel}}^{\text{rel}}(\omega') = \frac{2}{\pi} \frac{S_a(\omega')}{\omega'} d\omega' \quad (\text{S14})$$

The comparison from the spectral density analysis (SDA) and the NMA is shown in Fig. S8.

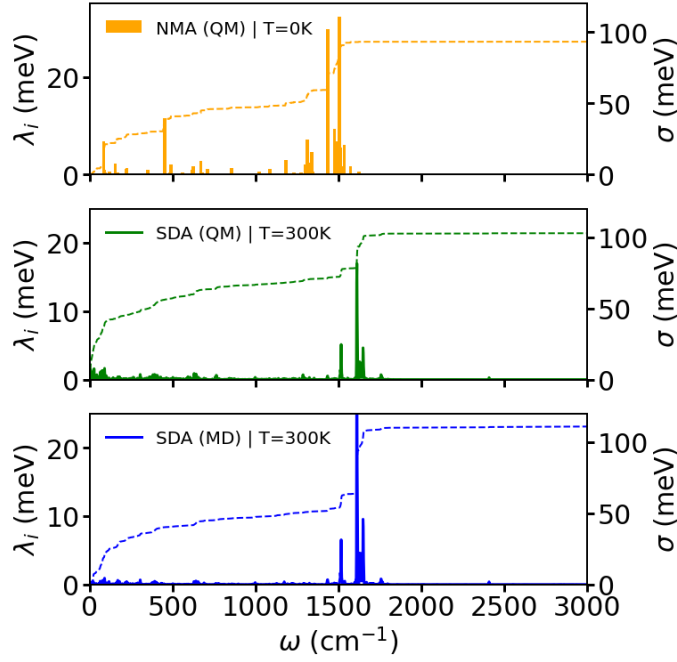


Figure S8: Relaxation energy (λ_i^{rel}) obtained from NMA (top panel) and the cosine transform of the excitation energies computed at QM and MD levels, middle and lower panels, respectively. Excitation energies of various snapshots extracted from MD were evaluated either using explicit TDDFT electronic structure calculations (green line) or using single point calculations performed using specifically parametrized QMD-FF for the ground and excited state of the molecule (blue line).

Section S9: QMD-FFs Potential energy expression.

All QMD-FFs were parameterized by partitioning the total energy of the system in an intramolecular term,^{26–28} governing the flexibility and shape of each monomer, and an intermolecular term, which describes the interactions among different monomers:

$$E_{\text{tot}}^{\text{QMD-FF}} = E_{\text{intra}}^{\text{QMD-FF}} + E_{\text{inter}}^{\text{QMD-FF}} \quad (\text{S15})$$

where,

$$E_{\text{intra}}^{\text{QMD-FF}} = \sum_k^{N_{\text{mon}}} E_k^{\text{intra}}, \quad E_{\text{inter}}^{\text{QMD-FF}} = \sum_{A \in k}^{N_{\text{at}}} \sum_{B \in l}^{N_{\text{at}}} E_{AB}^{\text{inter}} \quad (\text{S16})$$

with N_{mon} (N_{at}) being the number monomers (atoms) composing the systems, k and l indexes running over the atoms of two different monomers. For the QMD-FF intramolecular term we adopt a class I expression:

$$\begin{aligned}
E_k^{QMD-FF} = & \frac{1}{2} \sum_i^{N_{bonds}} k_i^s (r - r_0)^2 + \frac{1}{2} \sum_i^{N_{angles}} k_i^b (\theta - \theta_0)^2 + \frac{1}{2} \sum_i^{N_{dihedrals}^{stiff}} k_i^{ht} (\varphi - \varphi_0)^2 \\
& + \sum_{\mu}^{N_{dihedrals}^{flex}} \sum_j^{N_{cos\mu}} k_{j\mu}^{ft} (1 + \cos[n_{j\mu}\delta_{\mu} - \gamma_{j\mu}]) \\
& + \sum_i^{N_{at}} \sum_j^{N_{at}} \left[4\epsilon_{ij} \left[\left(\frac{\sigma_{ij}}{r_{ij}} \right)^{12} - \left(\frac{\sigma_{ij}}{r_{ij}} \right)^6 \right] + \frac{q_i q_j}{r_{ij}} \right]
\end{aligned} \tag{S17}$$

where the first three harmonic potentials terms refer to stiff internal coordinates, whereas the fourth term is employed for flexible dihedrals and the last term takes into account non-bonded contributions between interacting atom pairs within the same monomer (excluding interactions up to 1-4 distance). Similarly, we choose to express the intermolecular QMD-FF term through the standard sum of 12-6 Lennard-Jones (LJ) and charge-charge contributions:

$$E_{AB}^{inter} = 4\epsilon_{AB} \left[\left(\frac{\sigma_{AB}}{r_{AB}} \right)^{12} - \left(\frac{\sigma_{AB}}{r_{AB}} \right)^6 \right] + \frac{q_A q_B}{r_{AB}} \tag{S18}$$

Where, ϵ_{AB} and σ_{AB} are the LJ 12-6 parameters and q_A and q_B the point charges. It is worth mentioning that the intra- and intermolecular LJ parameter sets ϵ_{AB} (ϵ_{ij}) and σ_{AB} (σ_{ij}) may in principle take different values,^{27,29} as they describe the interaction of atoms within the same monomer or between two separate monomers, respectively. However, in this work we have assumed they are the same.

Section S10: Validation of the Joyce QMD-FFs against QM reference data

We assessed the quality of the intra-molecular QMD-FF through a set of validation tests. The first test involved an MM geometry optimization, where all internal coordinates (ICs) were optimized without any constraints. The comparison between QM and MM optimized geometries was conducted through visual analysis and by computing the standard deviation between the QM and MM optimized structures in terms of both internal (bond lengths, angles, dihedrals) and cartesian coordinates (see Fig. S9a). The latter RMSD was 0.138 Ang, which is quite small considering the large number of atoms in the system. Additionally, the MM normal modes can be computed from the QMD-FF Hessian matrix, along with the associated vibrational frequencies, and projected onto the reference QM data as shown in Fig S9b.

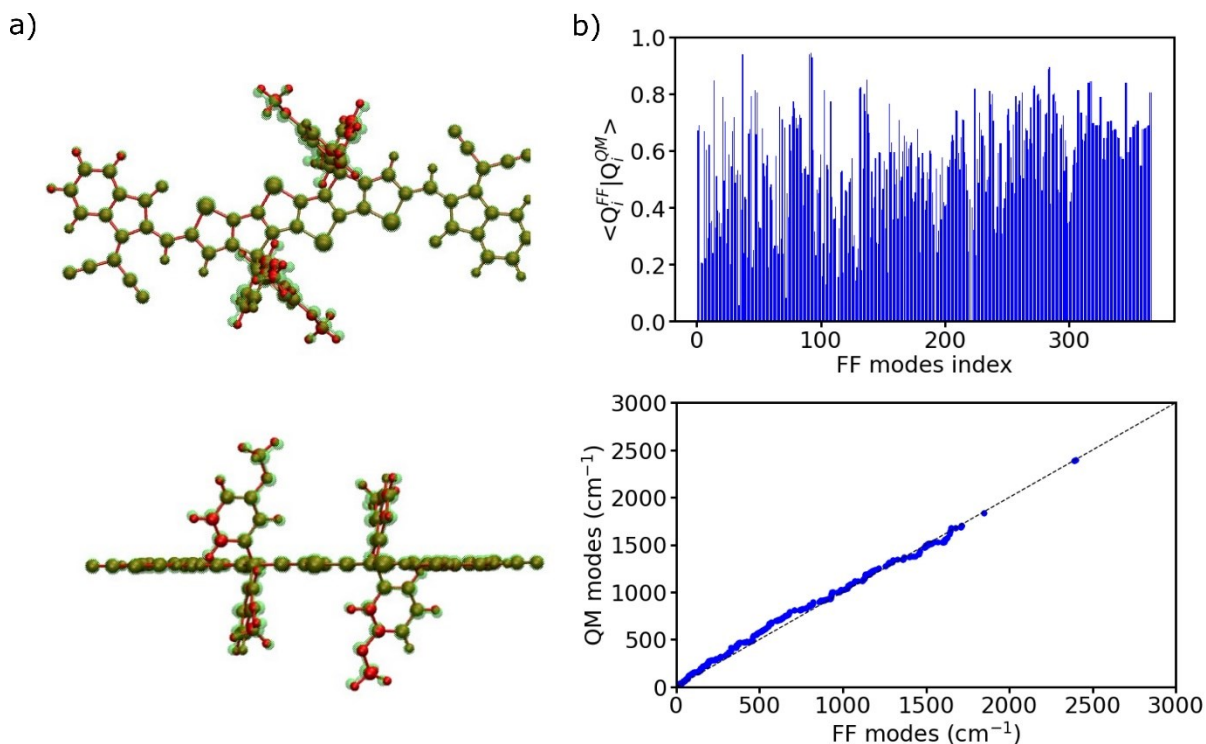


Figure S9: **a)** Superposition of QM (red) and MM (green) optimised geometries. **b)** Overlap of QM and MM normal modes (top), correlation plot between QM and MM vibrational frequencies computed with the QMD-FF (bottom).

Another validation test focuses on internal molecular flexibility and the ability of the MM description to accurately reproduce the torsional energy profile for each flexible dihedral δ_n . This aspect is evaluated through a comparison between the reference QM data and the MM torsional profile, obtained both using the QMD-FF within the Frozen Internal Rotation Approximation (FIRA)²⁷ or in a relaxed δ_n scan. We performed relaxed scans of the flexible dihedrals δ_n reported in Fig. 1 at the same level of theory. As shown in Fig. S10, all torsional QM profiles are well reproduced even using a fully relaxed scan of the potential performed at MM level. We used the Gaussian16 package for electronic wavefunction computations.

The quality of the intermolecular parameters was checked by comparing the Center of mass (COM) radial distribution function extracted along a 500 ps MD trajectory with the experimental crystal structure distribution. Result given in Fig. S11.

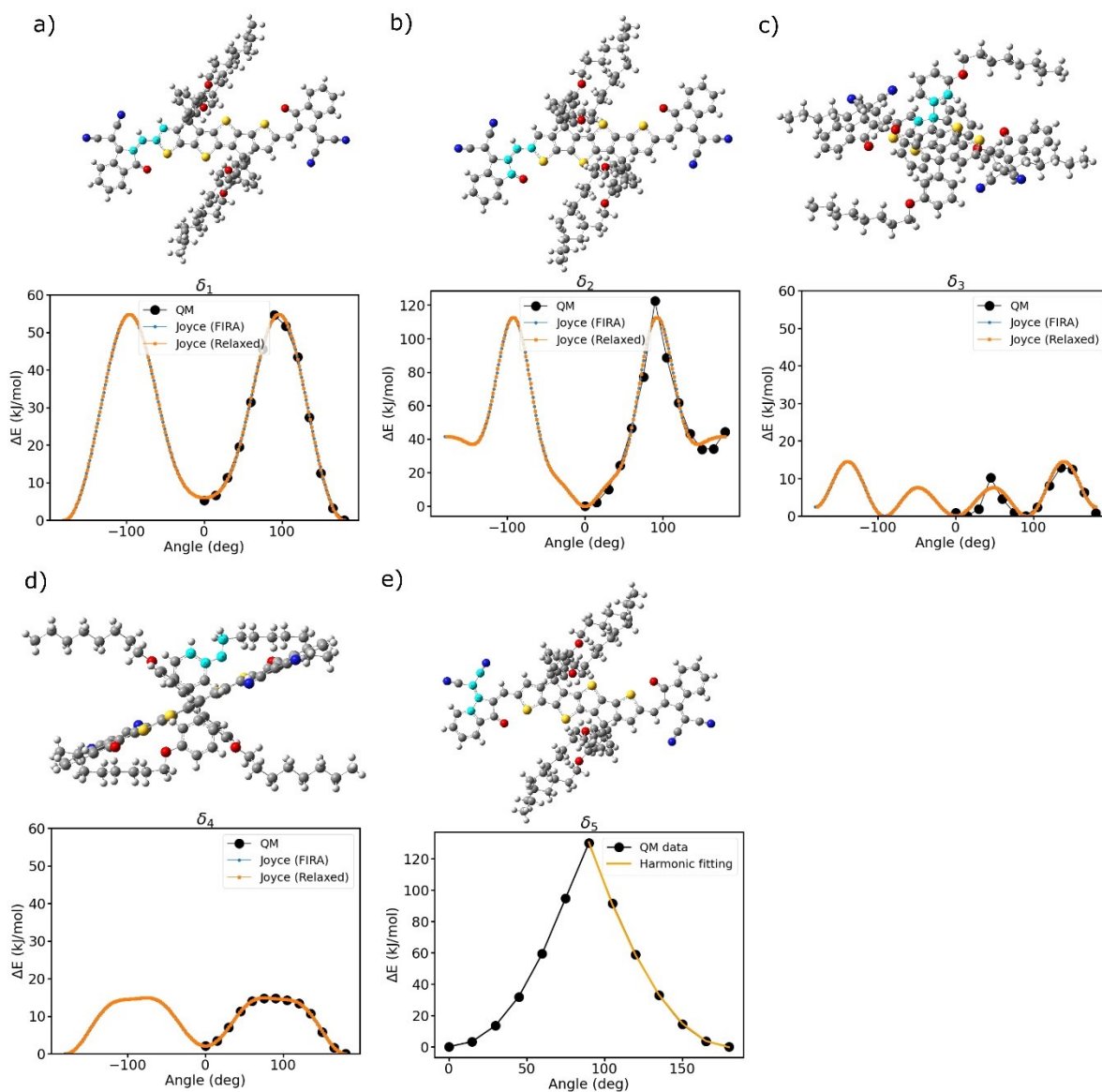


Figure S10: a)-d) QM (dots) and MM (dashed lines) potential energy profiles for δ_1 – δ_4 flexible dihedrals for m-4TICO. Frozen Internal Rotation Approximation (FIRA)^{26–28} is shown in blue, while relaxed potential energy scan in orange. e) δ_5 is fitted using a harmonic function. In all figures the scanned dihedrals are represented in cyan.

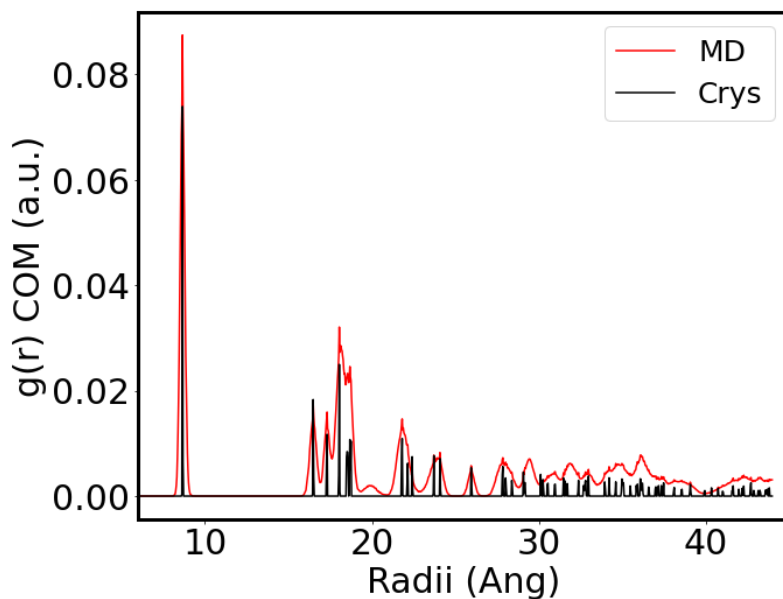


Figure S11: Structural validation of MD simulations of m-4TICO 20x20x2 supercell. (a) Molecular representation of C8-DNTT-C8 and atom indices as used in the other panels. (b) Center of mass (COM) radial distribution function (in arbitrary units) compared with experimental crystal structure

Section S11: Solid-state Aggregate Spectra with no off-diagonal disorder

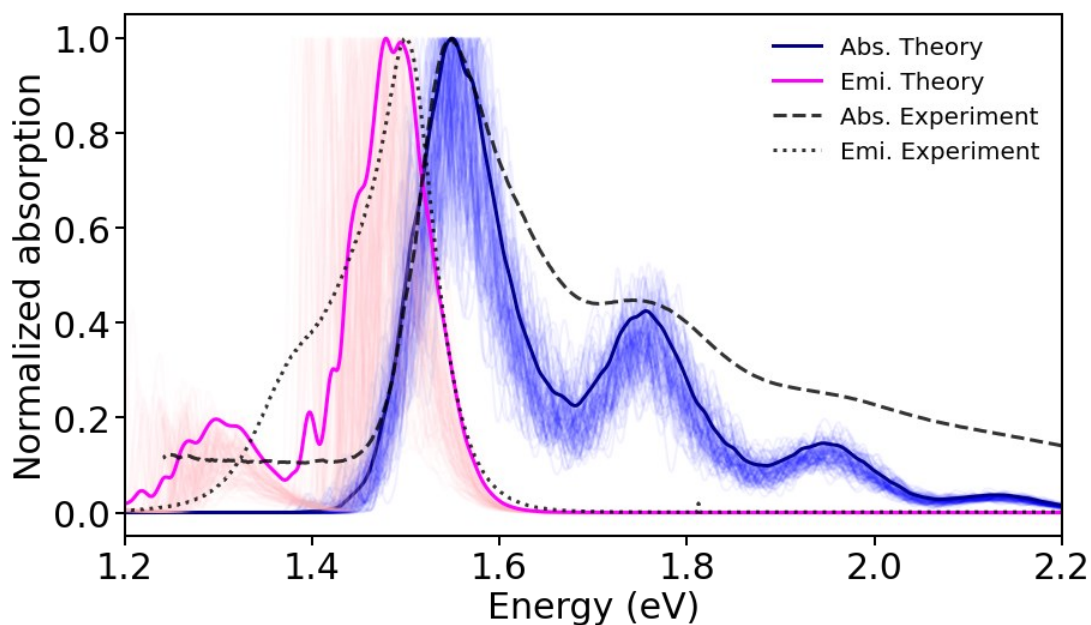


Figure S12: Computed absorption (solid blue line) and emission (solid magenta line) average spectra over 100 realizations of diagonal disorder as done in Fig. 3c of the main text. Off-diagonal disorder is not included in the spectra.

Section S12: Exciton diffusion

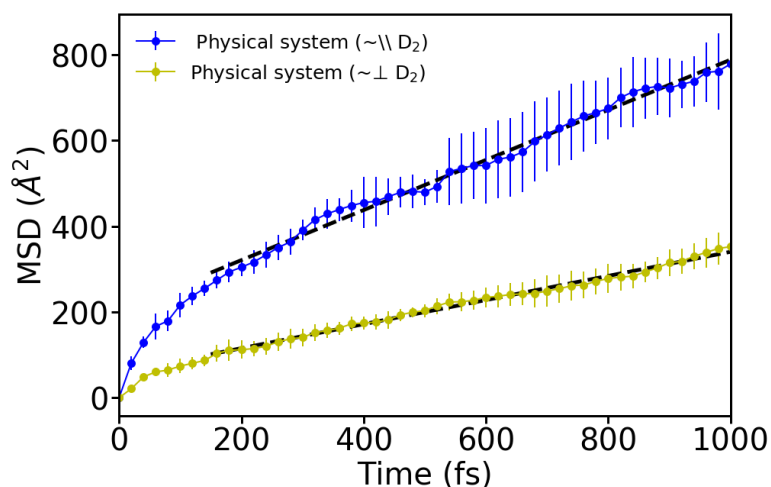


Figure S13: MSD of the exciton wavefunction along the eigendirections of the physical system. In blue we represent the MSD along the faster eigendirection oriented almost parallel to the D2 coupling pair. While in green we show the slower eigendirection perpendicular almost perpendicular to the D2 coupling pair direction. The MSD is averaged over 500 trajectories. Statistical error bars indicate the standard deviations over five independent blocks of 100 trajectories. Dashed black line represented the fitted region.

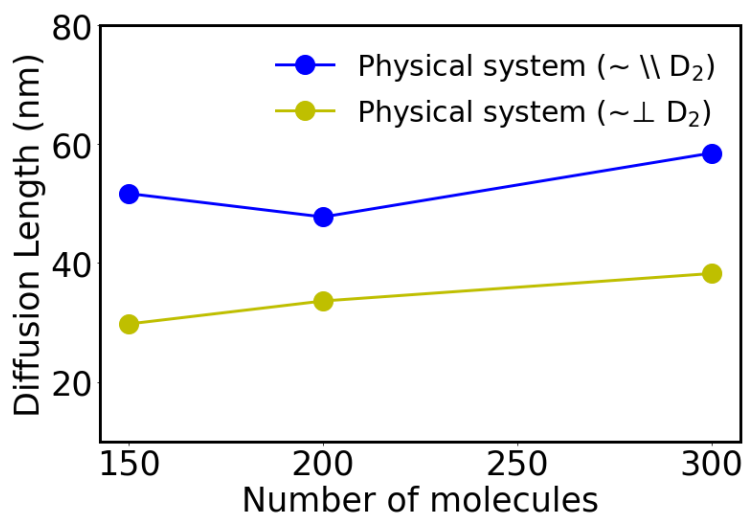


Figure S14: Convergence of the diffusion tensor for the physical system as a function of the number of electronically active molecules for the supercells. The eigendirection components parallel to D2 and perpendicular to it are shown in blue and yellow, respectively. The diffusion constant is obtained from linear fits to the MSD after initial relaxation, as described in the main text.

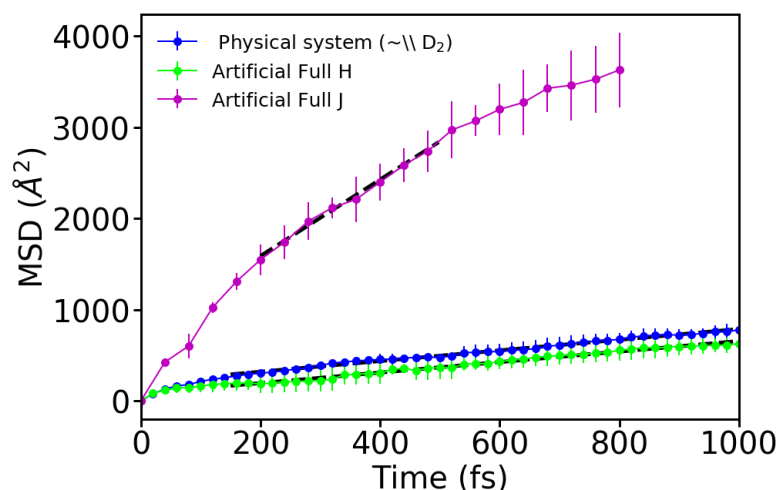


Figure S15: MSD of the exciton wavefunction along the eigendirections of the system for the three models presented in the main text. Only the eigendirection in the fast component is represented. The MSD is averaged over 500 trajectories. Statistical error bars indicate the standard deviations over five independent blocks of 100 trajectories. Dashed black line represented the fitted region. Note that the MSD of “Artificial Full J” system bends at longer time because the exciton wavefunction hits the boundary of the simulation box, thus the estimate of the corresponding diffusion coefficient might be unreliable.

References

- 1 T. Yanai, D. P. Tew and N. C. Handy, *Chem. Phys. Lett.*, 2004, **393**, 51–57.
- 2 V. Coropceanu, X.-K. Chen, T. Wang, Z. Zheng and J.-L. Brédas, *Nat. Rev. Mater.*, 2019, **4**, 689–707.
- 3 Z. Zheng, D. A. Egger, J.-L. Brédas, L. Kronik and V. Coropceanu, *J. Phys. Chem. Lett.*, 2017, **8**, 3277–3283.
- 4 A. J. Gillett, A. Privitera, R. Dilmurat, A. Karki, D. Qian, A. Pershin, G. Londi, W. K. Myers, J. Lee, J. Yuan, S.-J. Ko, M. K. Riede, F. Gao, G. C. Bazan, A. Rao, T.-Q. Nguyen, D. Beljonne and R. H. Friend, *Nature*, 2021, **597**, 666–671.
- 5 H. Oberhofer, K. Reuter and J. Blumberger, *Chem. Rev.*, 2017, **117**, 10319–10357.
- 6 V. Stehr, R. F. Fink, M. Tafipolski, C. Deibel and B. Engels, *Wiley Interdiscip. Rev. Comput. Mol. Sci.*, 2016, **6**, 694–720.
- 7 J. Cerezo and F. Santoro, *J. Comput. Chem.*, 2023, **44**, 626–643.
- 8 F. J. Avila Ferrer and F. Santoro, *Phys. Chem. Chem. Phys.*, 2012, **14**, 13549.
- 9 J. Aragón and A. Troisi, *Adv. Funct. Mater.*, 2016, **26**, 2316–2325.
- 10 N. J. Hestand and F. C. Spano, *Chem. Rev.*, 2018, **118**, 7069–7163.
- 11 S. Kashani, Z. Wang, C. Risko and H. Ade, *Mater. Horizons*, 2023, **10**, 443–453.
- 12 P. Mondelli, G. Boschetto, P. N. Horton, P. Tiwana, C. Skylaris, S. J. Coles, M. Krompiec and G. Morse, *Mater. Horizons*, 2020, **7**, 1062–1072.

- 13 F. C. Spano, *J. Chem. Phys.*, 2002, **116**, 5877–5891.
- 14 F. C. Spano, *Acc. Chem. Res.*, 2010, **43**, 429–439.
- 15 C.-P. Hsu, Z.-Q. You and H.-C. Chen, *J. Phys. Chem. C*, 2008, **112**, 1204–1212.
- 16 A. A. Voityuk, *J. Chem. Phys.*, 2006, **124**, 1–7.
- 17 C.-H. Yang and C.-P. Hsu, *J. Chem. Phys.*, 2013, **139**, 154104.
- 18 L. Cupellini, M. Corbella, B. Mennucci and C. Curutchet, *WIREs Comput. Mol. Sci.*, 2019, **9**, 1–23.
- 19 M. Nottoli, S. Jurinovich, L. Cupellini, A. T. Gardiner, R. Cogdell and B. Mennucci, *Photosynth. Res.*, 2018, **137**, 215–226.
- 20 J. Tölle, L. Cupellini, B. Mennucci and J. Neugebauer, *J. Chem. Phys.*, 2020, **153**, 184113.
- 21 S. Giannini, W.-T. Peng, L. Cupellini, D. Padula, A. Carof and J. Blumberger, *Nat. Commun.*, 2022, **13**, 2755.
- 22 S. Giannini, D. J. C. Sowood, J. Cerda, S. Frederix, J. Grune, G. Londi, T. Marsh, P. Ghosh, I. Duchemin, N. C. Greenham, K. Vandewal, G. D’Avino, A. J. Gillett and D. Beljonne, 2023, 1–31.
- 23 S. Mahadevan, T. Liu, S. M. Pratik, Y. Li, H. Y. Ho, S. Ouyang, X. Lu, H. Yip, P. C. Y. Chow, J. Brédas, V. Coropceanu, S. K. So and S.-W. Tsang, *Nat. Commun.*, 2024, **15**, 2393.
- 24 S. Giannini, A. Carof, M. Ellis, H. Yang, O. G. Ziogos, S. Ghosh and J. Blumberger, *Nat. Commun.*, 2019, **10**, 3843.
- 25 S. Giannini, O. G. Ziogos, A. Carof, M. Ellis and J. Blumberger, *Adv. Theory Simulations*, 2020, **3**, 2070021.
- 26 J. Cerezo, G. Prampolini and I. Cacelli, *Theor. Chem. Acc.*, 2018, **137**, 1–15.
- 27 I. Cacelli and G. Prampolini, *J. Chem. Theory Comput.*, 2007, **3**, 1803–1817.
- 28 D. Padula, A. Landi and G. Prampolini, *Energy Adv.*, 2023, **2**, 1215–1224.
- 29 J. G. Vilhena, L. Greff Da Silveira, P. R. Livotto, I. Cacelli and G. Prampolini, *J. Chem. Theory Comput.*, 2021, **17**, 4449–4464.